# Supplemental Material: Detection of cross-correlation between gravitational lensing and gamma rays

## GRAVITATIONAL LENSING DATA

The Dark Energy Survey (DES [13]) is a photometric survey performed with the Dark Energy Camera (DECam [14]) on the Blanco 4 m telescope at Cerro Tololo Inter-American Observatory (CTIO) in Chile. DES has observed approximately 5000 deg$^2$ of the Southern sky in five broadband filters, $g$, $r$, $i$, $z$, and $Y$, ranging from 400 to 1060 nm. The primary goal of DES is to study the origin of cosmic acceleration and the nature of dark energy through four key probes: weak lensing, clustering of the large-scale structure, galaxy clusters, and type Ia supernovae.

The first season of DES observations, from 31$^{\rm st}$ August 2013 to 9$^{\rm th}$ February 2014, resulted in the Y1 data stet analysed here [15, 16]. During Y1, DES observed $\sim$ 1500 deg$^2$ of the wide-area survey footprint with three to four dithered tilings per filter. The Y1 footprint consisted of two areas: one near the celestial equator including Stripe 82 (S82[17]), and a much larger area that was also observed by the South Pole Telescope (SPT[18]). In Fig. 1 of the main text we show with a solid white line the DES Y1 sky coverage in celestial coordinates; the complete sky coverage for the final survey is shown with a dashed line. Fig. 5 shows the DES Y1 footprint in Galactic coordinates.

In our analysis we make use of the METACALIBRATION shear catalogue [9]. The METACALIBRATION catalogue yields a total of 35 million objects and the final number density of the selection is 5.5 galaxies per square arcminute. METACALIBRATION [8, 19] is a method to estimate weak lensing shear, calibrating associated biases directly from the imaging data, rather than from prior information about galaxy properties or simulations. METACALIBRATION has been shown to be accurate at the part-per-thousand level in the absence of blending with other galaxies [8], and at the part-per-hundred level for the blending present in DES Y1 data [9].

The implementation of METACALIBRATION consists of measuring the two-component ellipticity, $\boldsymbol{e}$, of a galaxy in the DES Y1 run by fitting a single Gaussian model to its single-epoch images in the *riz* bands. The galaxy images are then artificially distorted with a known shear, $\boldsymbol{\gamma}$, and the ellipticity is measured again to construct the response matrix, $\boldsymbol{R}_\gamma$, as the derivative of measured ellipticity w.r.t. shear. Thus, the ellipticity estimator can be written as the following Taylor expansion [8, 9, 19]:

$$\boldsymbol{e} = \boldsymbol{e}|_{\gamma=0} + \frac{\partial \boldsymbol{e}}{\partial \boldsymbol{\gamma}} \boldsymbol{R}_{\gamma=0}\boldsymbol{\gamma} + \ldots = \boldsymbol{e}|_{\gamma=0} + \boldsymbol{R}_\gamma \boldsymbol{\gamma} + \ldots . \tag{1}$$

The elements of the response matrix are measured in METACALIBRATION by the numerical derivative:

$$\boldsymbol{R}_{\gamma_{i,j}} = \frac{e_i^+ - e_i^-}{\Delta\gamma_j}, \tag{2}$$

where $e_i^\pm$ is the measurement of the $i$th ellipticity component made on an image sheared by $\pm\gamma_j$, and $\Delta\gamma_j = 2\gamma_j$.

It is also necessary to correct for selection effects, i.e. shear biases that may occur when placing a cut on any quantities that change under shear, such as signal-to-noise ratio. This is accomplished by measuring the mean response of the estimator to the selection, repeating the selections on quantities measured on sheared images. The mean selection response matrix is given by:

$$\langle \boldsymbol{R}_{S_{i,j}} \rangle = \frac{\langle e_i^{S+} \rangle - \langle e_i^{S-} \rangle}{\Delta\gamma_j}, \tag{3}$$

where $\langle e_i^{S\pm} \rangle$ represent the mean of the ellipticities measured on images without artificial shearing, but selected by properties measured on sheared images. The full response for the mean shear is given by the sum of the shear response and selection response:

$$\langle \boldsymbol{R} \rangle = \langle \boldsymbol{R}_\gamma \rangle + \langle \boldsymbol{R}_S \rangle. \tag{4}$$

When measuring a shear statistics, such as mean shear or a shear two-point function, the measurement can be appropriately corrected for the mean response $R = (\langle \boldsymbol{R} \rangle_{11} + \langle \boldsymbol{R} \rangle_{22})/2$ to produce a calibrated result.

DES galaxies were assigned to redshift bins using a re-implementation of the BPZ algorithm [20], which provides an estimate of the redshift probability density $p_{\rm BPZ}(z_j)$ of each galaxy $j$. The assignment is done based on fluxes measured by METACALIBRATION on the original and sheared images to correct for selection response of redshift

binning. The fluxes in the bands *griz* of the METACALIBRATION galaxies are used for estimating an expectation value of $\langle z \rangle = \int_0^z z_j \mathrm{d}z_j \, p_{\rm BPZ}(z_j)$. Thus, four redshift bins are defined by $0.20 < \langle z \rangle < 0.43$, $0.43 < \langle z \rangle < 0.63$, $0.63 < \langle z \rangle < 0.90$, and $0.90 < \langle z \rangle < 1.30$. The corresponding four redshift distributions, $n^i(z)$, are taken as the stacked $p_{\rm BPZ}(z)$ of the galaxies, estimated from their improved joint-fit photometry [16, 21]. The mean values of each redshift bin stacked $p_{\rm BPZ}(z)$ are calibrated independently, and they are found to be consistent with the BPZ estimate, with a joint uncertainty of $\sigma_{\langle z \rangle} \approx 0.015$ [21].

Since the purpose of this work is detection of the cross-correlation between the UGRB and shear, rather than accurate constraints on cosmological parameters, we do not explicitly account for the systematic uncertainties in shear and redshift calibration in our analysis. The moderate significance of our measurements and the accuracy of the DES Y1 calibrations justify this choice.

## GAMMA-RAY DATA

*Fermi*-LAT is a $\gamma$-ray pair-conversion telescope that has been operating for the last 10 years in space. Due to its wide energy range (20 MeV to 1 TeV) and its capability of rejecting the background of charged cosmic rays, it is an excellent instrument to investigate the UGRB. It scans the whole sky every three hours with a remarkable angular resolution for $\gamma$ rays ($\sim 0.1$ deg above 10 GeV).

In this work we used 108 months of data, from mission week 9 to week 476. The photon and exposure maps are produced with the LAT Science Tools version `v10r0p5` [52]. We selected the Pass8 ULTRACLEANVETO class [53], which has the lowest cosmic-ray contamination and is the most appropriate class for diffuse emission analysis. The Fermi Tools provide the possibility of choosing different angular resolutions, which are organised in four quartiles, from PSF0 to PSF3, corresponding to a transition from the worst to the best PSF. In order to have a balance between the photon count statistics and a good direction reconstruction, we selected the best quartile PSF3 for energies below 1.2 GeV (where we have the highest photon counts) and PSF1+2+3 for higher energies. The PSF is modelled according the *Fermi*-LAT specifications [54] and for each energy bin in our analysis an effective PSF is determined by weighting the energy-dependent PSF by the intensity energy spectrum of the UGRB.

We produced 100 intensity maps in `HEALPix` projection with $N_{\rm side} = 1024$, evenly spaced in logarithmic scale between 100 MeV and 1 TeV, by dividing the count maps by the exposure and the pixel area. The size of such energy bins is small enough that the exposure can be approximated by its mean value within the energy bin when deriving the flux. The resulting flux maps are then re-binned into 9 larger energy bins between 631 MeV to 1 TeV by simply adding up fluxes from the smaller bins. We discard very low energies because the angular resolution is too poor for our purposes.

Since we are interested only in the UGRB, we benefit from excluding Galactic emission and resolved point sources. This is achieved by a process of masking and subtracting described below.

### Masking $\gamma$-ray data

We build a set of masks according to the following two criteria:

1. Low latitudes, where the Galactic foreground is stronger, are removed by a flat cut excluding the region between $\pm 30$ deg of latitude.

2. Sources identified in the list FL8Y are masked. FLY8 [55] has been recently released by the *Fermi*-LAT Collaboration as a preliminary version of the upcoming 4FGL catalogue. It contains 5523 sources. Above 10 GeV, we mask also the sources which are present in the 3FHL catalogue [22], that is more accurate for high energy sources. Each source is masked taking into account both its source brightness and the detector PSF resolution in the specific energy bin. The masking radius $R$ has been defined by:

$$F^g_{\Delta E} \exp\left(-\frac{R^2}{2\theta^2_{\Delta E}}\right) > \frac{F^g_{\Delta E,\rm faintest}}{5} \tag{5}$$

where $F^g_{\Delta E}$ is the integral flux of the source in a given energy bin $\Delta E$, $F^g_{\Delta E,\rm faintest}$ is the flux of the faintest source in the same energy bin (and once divided by 5 provides an approximate estimate of the noise, i.e., the faintest source emission is approximately a measure of the $5\sigma$ level), and $\theta_{\Delta E}$ is the 68% containment angle in that energy bin, as provided by the *Fermi*-LAT PSF. We verified that the non-Gaussian tail of the PSF (not included in the Gaussian approximation in Eq. (5)) does not appreciably contaminate our maps.

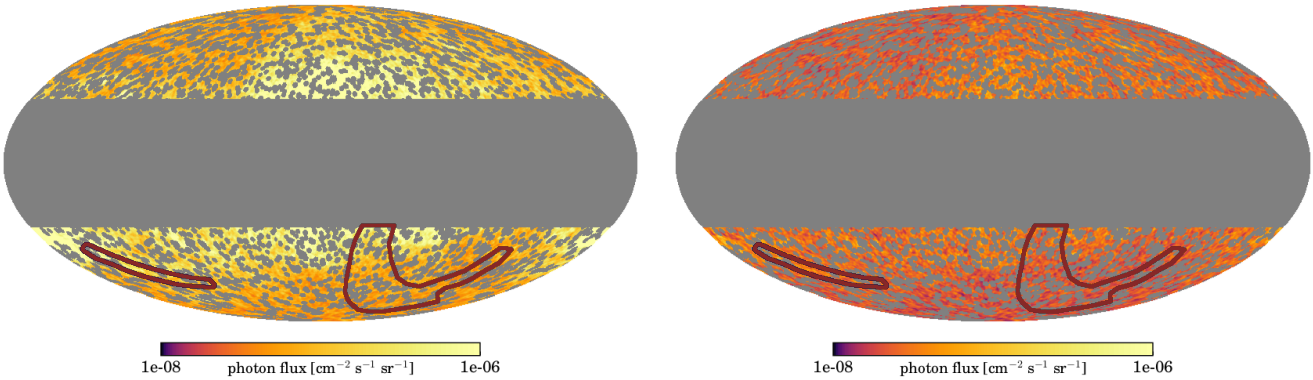


FIG. 5: Masked $\gamma$-ray map in the $(1.2-2.3)$ GeV energy bin before (left) and after (right) the foreground subtraction. The maps have been downsized to $N_{\rm side}=128$ and smoothed with a Gaussian beam of size $\sigma=0.4^\circ$ for illustration purposes. The DES Y1 sky footprint is shown with red solid line.

This strategy aims at masking the Galactic plane and resolved sources over a sufficiently large area, in order to reduce the chance to have artefacts in the APS produced by source leakage and foreground emission. For further details and impact of the mask, see also ref. [10].

### Foreground removal

Despite the majority of the Galactic foreground has been removed by cutting out the Galactic plane, still high-latitudes might contain some contamination that causes noise in our analysis. While galactic emission does not contribute to the cross-correlation signal with gravitational shear, nevertheless a foreground contamination adds to the error budget. We therefore performed a galactic foreground subtraction by adopting the template maps provided by the *Fermi*-LAT Collaboration with the Galactic emission model `gll_iem_v06.fits` [56]. The foreground template is projected in HEALPix maps with the same $N_{side}$ as the intensity maps and in the same 100 energy bins. Each template map is convolved with the *Fermi*-LAT PSF and assigned a free normalization. This component is added to a free constant (representing the UGRB and cosmic-ray contamination) and a Poissonian likelihood fit is performed globally on all the masked intensity maps. All obtained best-fit normalization parameters are of the order of unity, supporting a successful description of the foreground emission. The normalised foreground templates are then re-binned into the 9 larger energy bins and subtracted from the corresponding intensity maps.

In Fig. 5, we show an example of the *Fermi*-LAT $\gamma$-ray intensity map in the (1.2-2.3) GeV energy bin with the application of the mask described above and illustrating the effect of the Galactic foreground subtraction.

The impact of foreground removal in cross-correlation studies involving $\gamma$-rays has been discussed in Refs. [3, 4, 6, 32, 50], where it was shown that the effect is marginal. As mentioned, the main effect of foreground residuals on our study would be a mild reduction of detection significance. This can be appreciated in Fig. 6, where we show the analogous of Fig. 2 of the main text, but without foreground removal. Since the amplitude $\Xi$ is dimensionless, in Fig. 6 it has been normalized as in Fig. 2 of the main text (i.e. relative to the mean intensity $\langle I_\gamma\rangle$ of the foreground-subracted maps), to allow a direct comparison of the two plots. Put in different words, this implies that the dimensional correlation function is the same when determined on subtracted or unsubtracted maps (with larger errors in the latter case).

## ESTIMATION OF THE COVARIANCE MATRIX

The covariance matrix is estimated by combining the theoretical Gaussian large-scale structure covariance with realizations of the shape-noise term generated from the data. The latter term is expected to be dominating in the covariance, while the former should be small. To avoid notation conflict between the symbol $\gamma$ usually employed for both the weak lensing effect of gravitational shear, and for $\gamma$-rays, we shall here simply refer to shear through indexes $r,s$, labelling redshift bins, and to the UGRB anisotropies via indexes $a,b$, labelling energy bins.

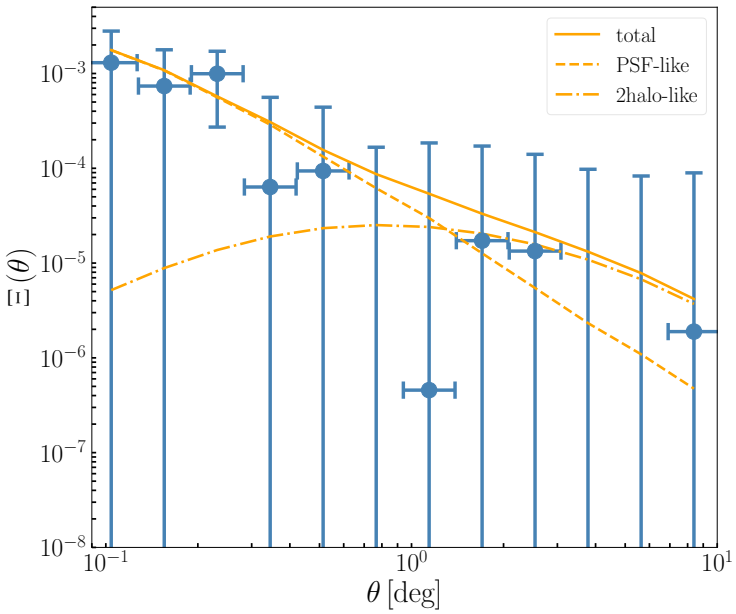


FIG. 6: Same as Fig. 2 of the main text but without foreground removal (and normalized as in Fig. 2 of the main text, being $\Xi$ dimensionless).

In the Gaussian approximation, the generic element of the theoretical harmonic-space covariance matrix $\widehat{\mathbf{\Gamma}}$ reads:

$$\widehat{\Gamma}_{ar\ell,bs\ell'} = \frac{\delta^{\rm K}_{\ell\ell'}}{(2\ell+1)\Delta\ell f_{\rm sky}}\left[C^{ar}_{\ell}C^{bs}_{\ell'} + \left(C^{rs}_{\ell'}+\mathcal{N}^{rs}\right)\left(C^{ab}_{\ell}+\mathcal{N}^{ab}\right)\right]. \tag{6}$$

It represents the covariance between the measurements of two cross-correlation harmonic-space power spectra: one cross-correlating $\gamma$-ray map in energy bin $a$ with shear map in redshift bin $r$; and another considering $\gamma$-ray map in energy bin $b$ with shear map in redshift bin $s$. In the Gaussian approximation, these two cross-correlation power spectra, $C^{ar}_{\ell}$ and $C^{bs}_{\ell'}$, have a covariance which is diagonal in $\ell\ell'$, and which depends on both the cross-correlation signals, as well as the $\gamma$-ray–$\gamma$-ray and shear-shear auto-correlations, i.e. $C^{ab}_{\ell}$ and $C^{rs}_{\ell'}$. Both auto and cross-correlation theoretical signals involving $\gamma$-rays have been corrected for the effect of the *Fermi*-LAT PSF beam function. In Eq. (6), $\mathcal{N}$ denotes the noise terms. Note that the noise does not depend on the angular scale. In Eq. (6) $f_{\rm sky}$ accounts for the incomplete sky coverage, with $f^{\rm DES}_{\rm sky} = 0.042$ denoting the DES footprint (independent of the redshift bin) and $f^{a}_{\rm sky} = (0.315, 0.289, 0.404, 0.449, 0.468, 0.475, 0.476, 0.477, 0.477)$ being the fraction of unmasked pixels of the $\gamma$-ray map in the $a$-th energy bin. For the cross-correlation estimator with complex masks as we have here, an unambiguous definition of $f_{\rm sky}$ is not possible. We tested two options: a geometric mean $f_{\rm sky} = (f^{a}_{\rm sky}f^{\rm DES}_{\rm sky})^{1/2}$ and the $f_{\rm sky}$ relative to the overlap of the DES footprint with the *Fermi*-LAT unmasked sky. We comment more in the two alternatives below, but we anticipate that results on the SNR arising from the two choices exhibit only a minor change.

For details on the Gaussian covariance matrix, see Section 5.1 in ref. [2]. Since our measurements are performed in real space, we compute the Legendre transform of Eq. (6) to return the real-space covariance matrix, $\mathbf{\Gamma}$, with entries $\Gamma_{ar\vartheta,bs\vartheta'}$.

As mentioned above, the dominant contribution to the covariance is represented by the shape noise term. In the Gaussian approximation, it takes the form of $\mathcal{N}^{rs}(C^{ab}_{\ell}+\mathcal{N}^{ab})$. In order to estimate this contribution more accurately, without resorting to theoretical approximations, we produce 2000 realisations of the noise directly from the data in real space. To this end, we rotate each galaxy in our catalogue by an independent random angle. The shear signal as measured from these rotated source catalogues represents a random realisation of shape noise (see e.g. refs. [7, 23, 24]).

We complete the construction of the total covariance by adding a theoretical estimate of the large-scale structure term, $C^{ar}_{\ell}C^{bs}_{\ell}+C^{rs}_{\ell}(C^{ab}_{\ell}+\mathcal{N}^{ab})$. We assume it subdominant in the covariance budget, and this is verified a posteriori. The $\gamma$-ray auto-correlation $C^{ab}_{\ell}$ entering in the theoretical estimate can be well-fitted by a simple model, given by a power-law plus a constant, i.e. $C^{ab}_{\ell,\rm mod} = A_{ab}\ell^{-\alpha_{ab}}+C^{ab}_{\rm P}$ (see e.g. ref. [10]). We fit the three parameters $\{A_{ab}, \alpha_{ab}, C^{ab}_{\rm P}\}$ for each energy bin pair against the measurement of the auto-correlation power spectrum obtained by running the

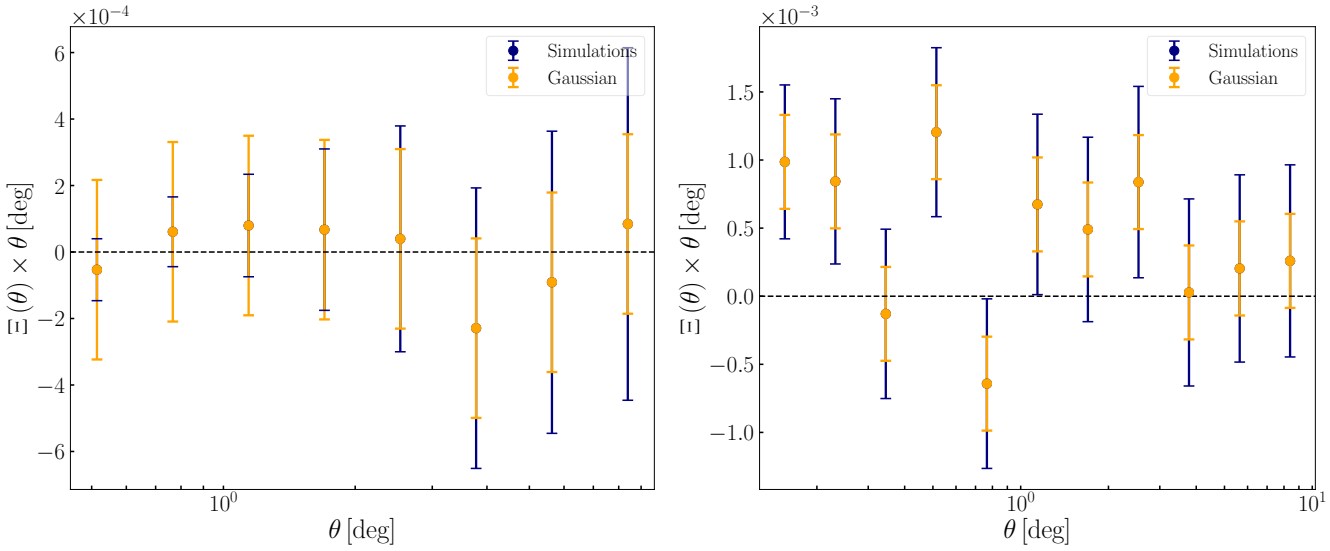


FIG. 7: Comparison between the shape-noise standard deviation computed with the theoretical Gaussian approximation (yellow error bars) and via the simulations (blue error bars) for two energy bins in the first DES redshift bin. We focus only on angular scales above the *Fermi*-LAT PSF in the specific energy bin. *Left panel:* energy bin between 1.2 and 2.3 GeV. *Right panel:* energy bin between 131 and 1000 GeV.

tool `PolSpice` (as in ref. [10]). Finally, the $\gamma$-ray noise term, $\mathcal{N}^{ab}$, is computed with the analytic estimator of eq. 5 in ref. [25].

The shear auto-correlation is derived using the galaxy redshift distributions described above, and adopting $\Lambda$CDM cosmology with parameter fiducial values from *Planck* [26]. The model is compatible with previous measurements [27].

The large-scale structure part of the covariance is added to the shape noise term by using the following procedure. We create a set of 2000 simulated datasets from a multivariate Gaussian distribution with zero mean and covariance equal to the large-scale structure part of the theoretical covariance. Then, we add this simulated data to the shape noise realisations discussed above, thus obtaining 2000 samples containing both terms. These 2000 samples are then used to obtain the covariance matrix. The inverse of the covariance estimated such is a biased estimator of the inverse covariance, with the bias depending on the number of realisations, number of bins, and parameters of the model chosen to fit the data [28, 29]. We apply the Anderson-Hartlap correction in order to de-bias the inverse covariance (as done e.g. in Section 3 of ref. [30]).

In order to validate our procedure, we compare the shape noise term obtained via the simulations with the analogous term from the theoretical estimate, $\mathcal{N}^{rs}(C_\ell^{ab} + \mathcal{N}^{ab})$. In Fig. 7, we show a comparison between the theoretical shape noise standard deviation and the results from the simulations, in the case of a low-energy bin (left panel) and a high-energy bin (right panel) combined with the lowest DES redshift bin. We see that the variance obtained with the two techniques approximately agrees, yet can differ due to complex masking effects present in the data [31]. When deviations are present, the variance obtained with simulations is typically larger, as expected. By adopting the shape noise term directly derived from the data, we ensure that the quoted errors and values for the goodness of fit are correct.

We compare also the large-scale structure term with the covariance matrix obtained from simulations after rescaling the latter by $C_\ell^{rs}/\mathcal{N}^{rs}$. Results are in very good agreement with the choice of the effective parameter $f_{\rm sky}$ entering Eq. (6) as the geometric mean of DES and *Fermi*-LAT sky coverage. Another value for the $f_{\rm sky}$ parameter that is frequently used in the literature is the overlap between the two masks. We verified that, in this case, results would be just slightly modified, with the SNR becoming 4.8 instead of 5.3, as obtained in the main analysis.

## THEORETICAL MODELS

The harmonic-space (often referred to as 'angular') power spectrum of the cross-correlation between a map of $\gamma$-rays in the $a$th energy bin and a map of gravitational shear in the $r$th redshift bin can be computed as:

$$C_\ell^{ar} = \int \mathrm{d}E\,\mathrm{d}z\,\frac{1}{H(z)}\frac{W^a_{\rm gamma}(E,z)W^r_{\rm shear}(z)}{\chi(z)^2}P_{\gamma\delta}\left[k=\frac{\ell}{\chi(z)},z\right], \tag{7}$$

where $E$ is the $\gamma$-ray energy, and $\chi(z)$ is the comoving distance to redshift $z$, obeying $\mathrm{d}z/\mathrm{d}\chi = H(z)$ with $H(z)$ the Hubble rate. Formally, the integrals extend over the whole $\gamma$-ray energy spectrum and from $z = 0$ to the horizon, but the window functions $W^a_{\rm gamma}(E,z)$ and $W^r_{\rm shear}(z)$ implement energy and redshift binning effectively reducing the integration range (for details, see next Subsections). Finally, $P_{\gamma\delta}$ is the three-dimensional cross-power spectrum between a given $\gamma$-ray population sourcing the UGRB emission and the matter density contrast $\delta$. It represents the three-dimensional correlation (in Fourier space) between what seeds the unresolved $\gamma$-ray emission and what sources the gravitational lensing effect, namely matter inhomogeneities. It is a function of both redshift and physical scale $k$, the modulus of the physical wavenumber. In the Limber approximation, $k$ and the angular multipole $\ell$ are linked by $k = \ell/\chi(z)$. This approximation is valid for $\ell \gg 1$, which is the case of the present work.

As mentioned before, the quantity measured from the data is the real-space cross-correlation of UGRB anisotropies with tangential shear, which is related to the harmonic-space cross-power spectrum of Eq. (7) by a Legendre transform:

$$\hat{\Xi}^{ar}(\theta) = \sum_\ell \frac{2\ell+1}{4\pi\ell(\ell+1)} C_\ell^{ar}\, W_\ell^a\, P_\ell^{(2)}(\cos\theta), \tag{8}$$

with $\theta$ being the angular separation on the sky, $P_\ell^{(2)}$ the Legendre polynomial of order two, and $W_\ell^a$ the *Fermi*-LAT PSF beam function in energy bin $a$, accounting for the finite resolution of the detector.

### Gravitational lensing window function

The window function describes the mean distribution of the signal along the line of sight, in the given energy or redshift bin. For the gravitational lensing effect, the window function is given by (see e.g. ref. [33]):

$$W^r_{\rm shear}(z) = \frac{3}{2}H_0^2\Omega_{\rm m}(1+z)\chi(z)\int_z^\infty \mathrm{d}z'\,\frac{\chi(z')-\chi(z)}{\chi(z')}n^r(z'), \tag{9}$$

where $H_0 \equiv H(z=0)$ is the Hubble constant, $\Omega_{\rm m}$ is the matter abundance in the Universe (sum of the dark matter and the baryon abundances, $\Omega_{\rm DM}$ and $\Omega_{\rm b}$), and $n^r(z)$ is the redshift distribution of background galaxies in the lensing data set in bin $r$. The galaxy distribution depends on the data set and redshift cut, as described above.

### WIMP-sourced $\gamma$-rays window function

The window function for UGRB anisotropies sourced by annihilations of dark matter particles reads [1, 34]:

$$W^a_{\rm gamma,DM}(E,z) = \frac{(\Omega_{\rm DM}\rho_{\rm c})^2}{4\pi}\frac{\langle\sigma_{\rm ann}v\rangle}{2m^2_{\rm DM}}(1+z)^3\,\Delta^2(z)\frac{\mathrm{d}N_{\rm ann}}{\mathrm{d}E}\left[E(1+z)\right]e^{-\tau[E(1+z),z]}\,, \tag{10}$$

where $\rho_{\rm c}$ is the critical density of the Universe, $m_{\rm DM}$ is the mass of the dark matter particle, and $\langle\sigma_{\rm ann}v\rangle$ denotes the velocity-averaged annihilation cross-section, assumed here to be the same in all dark matter haloes.

Among the other ingredients, we have $\mathrm{d}N_{\rm ann}/\mathrm{d}E$, indicating the number of photons produced per annihilation as a function of energy, and setting the $\gamma$-ray energy spectrum. We will consider it to be given by the sum of two contributions: prompt $\gamma$-ray production from dark matter annihilations (or decays); and inverse Compton scattering of dark matter produced electrons and positrons on CMB photons (we compute inverse Compton assuming negligible magnetic field and no diffusion for the produced electrons and positrons). Results of our analysis will be shown for two annihilation final states: $b\bar{b}$ pairs, which yield a relatively soft spectrum of photons and electrons, mostly associated to hadronisation into pions and their subsequent decay; $\tau^+\tau^-$, which provides a harder spectrum, mostly associated to final state radiation of photons and decay of the muons produced by $\tau$ decay into electrons (with subsequent $\gamma$-ray emission through inverse Compton on CMB), with an additional semi-hadronic decay into pions [35–37].

Then, the optical depth $\tau$ in Eq. (10) accounts for attenuation of $\gamma$-rays by the extra-galactic background light, and is taken from the literature[38]. Finally, the clumping factor $\Delta^2$ is related to the fact that the signal of annihilating dark matter depends on the average of the square of the dark matter density; it is defined as (see e.g. ref. [1]):

$$\Delta^2(z) \equiv \frac{\langle \rho^2_{\rm DM} \rangle}{\bar{\rho}^2_{\rm DM}} = \int_{M_{\rm min}}^{M_{\rm max}} {\rm d}M \frac{{\rm d}n_{\rm h}}{{\rm d}M}(M,z)\,[1+b_{\rm sub}(M,z)] \times \int {\rm d}^3x\, \frac{\rho^2_{\rm h}(\boldsymbol{x}|M,z)}{\bar{\rho}^2_{\rm DM}}, \tag{11}$$

where: ${\rm d}n_{\rm h}/{\rm d}M$ is the halo mass function [39]; $M_{\rm min}$ is the minimal halo mass, which we fix to $10^{-6}M_\odot$; $M_{\rm max}$ is the maximal mass of haloes, for which we use $10^{18}M_\odot$, although results are insensitive to the precise value assumed; $\rho_{\rm h}(\boldsymbol{x}|M,z)$ is the dark matter density profile of a halo with mass $M$ at redshift $z$, taken to follow a Navarro-Frenk-White profile [40]; and $b_{\rm sub}$ encodes the 'boost' to the halo emission provided by subhaloes. To characterise the halo profile and the subhalo contribution, we need to specify their mass concentration. For the main haloes we follow ref. [41]. On the other hand, the description of the concentration parameter $c(M,z)$ at small masses and for subhaloes is still an open issue and provides a source of uncertainty. We considered the two most updated analyses, from Ref. [11], where we assume ${\rm d}n_{\rm sub}/{\rm d}M_{\rm sub} \propto M_{\rm sub}^{-2}$ (see also Ref. [42]), and from Ref. [12]. We show only the former, since the two descriptions just differ by roughly a constant factor (around 10) in the derived final value of the annihilation cross section.

*Astrophysical $\gamma$-ray sources window function*

Besides the possible particle dark matter emission, $\gamma$-rays in the UGRB are certainly produced by a number of astrophysical sources. The most relevant $\gamma$-ray emitters include: blazars, misaligned active galactic nuclei, and star forming galaxies. Their window function is given by:

$$W^a_{\rm gamma,S}(E,z) = \chi(z)^2 \int_{\mathcal{L}_{\rm min}}^{\mathcal{L}_{\rm max}(F_{\rm sens},z)} {\rm d}\mathcal{L}\, \Phi_{\rm S}(\mathcal{L},z,E)\, \frac{{\rm d}N_{\rm S}}{{\rm d}E}(\mathcal{L},z) \times e^{-\tau[E(1+z),z]}\,, \tag{12}$$

where $\mathcal{L}$ is the $\gamma$-ray rest-frame luminosity in the energy interval 0.1 to 100 GeV, $\Phi_{\rm S}$ is the $\gamma$-ray luminosity function (GLF) of the source class S of astrophysical emitters included in our analysis, and ${\rm d}N_{\rm S}/{\rm d}E$ is its observed (unabsorbed) energy spectrum. The upper bound, $\mathcal{L}_{\rm max}(F_{\rm sens},z)$, is the luminosity above which an object is resolved in the FL8Y and 3FHL catalogues, and consequently masked in our analysis. As we are interested in the contribution from unresolved astrophysical sources, only sources with luminosity smaller than $\mathcal{L}_{\rm max}$ are included. Conversely, the minimum luminosity, $\mathcal{L}_{\rm min}$, depends on the properties of the source class under consideration.

We consider a unified blazar model combining BL Lacertae and flat-spectrum radio quasars as a single source class. The GLF and energy spectrum are taken from ref. [43] where they are derived from a fit to the properties of resolved blazars in the third *Fermi*-LAT catalogue [44]. In the case of misaligned AGNs, we follow ref. [45], who built the GLF from the radio luminosity function of misaligned AGNs. We consider their best-fitting relation between the $\gamma$-ray and radio luminosities $\mathcal{L}$ -$L_{r,\rm core}$ and assume a power-law spectrum with index $\alpha_{\rm mAGN} = 2.37$. To derive the GLF of star-forming galaxies, we start from the infrared luminosity function [46] (adding up spiral, starburst, and SF-AGN populations of their Table 8). Then we relate $\gamma$-ray and infrared luminosities using the best-fitting $\mathcal{L}$-$L_{\rm IR}$ relation from ref. [47]. The energy spectrum is taken to be a power-law with spectral index $\alpha_{\rm SFG} = 2.7$.

**Three-dimensional seed power spectra**

To compute the three-dimensional cross-power spectrum $P_{\gamma\delta}$ between the clustering of a given population of $\gamma$-ray emitters and the matter density field, we follow the halo model formalism (e.g. ref. [48]), and write $P_{\gamma\delta} = P^{\rm 1h}_{\gamma\delta} + P^{\rm 2h}_{\gamma\delta}$. Below we derive the 1- and 2-halo terms for the various cases (see also ref. [1]).

*Dark matter $\gamma$-ray sources*

The 3D cross power spectrum between $\gamma$-ray emission from particle dark matter and matter density is given by:

$$P^{1\mathrm{h}}_{\gamma_{\mathrm{DM}}\delta}(k,z) = \int_{M_{\mathrm{min}}}^{M_{\mathrm{max}}} \mathrm{d}M \, \frac{\mathrm{d}n_{\mathrm{h}}}{\mathrm{d}M}(M,z) \, \hat{v}_{\gamma_{\mathrm{DM}}}(k|M,z) \, \hat{u}_{\delta}(k|M,z) \tag{13}$$

$$P^{2\mathrm{h}}_{\gamma_{\mathrm{DM}}\delta}(k,z) = \left[\int_{M_{\mathrm{min}}}^{M_{\mathrm{max}}} \mathrm{d}M \, \frac{\mathrm{d}n_{\mathrm{h}}}{\mathrm{d}M}(M,z) \, b_{\mathrm{h}}(M,z) \, \hat{v}_{\gamma_{\mathrm{DM}}}(k|M,z)\right] \left[\int_{M_{\mathrm{min}}}^{M_{\mathrm{max}}} \mathrm{d}M \, \frac{\mathrm{d}n_{\mathrm{h}}}{\mathrm{d}M}(M,z) \, b_{\mathrm{h}}(M,z) \hat{u}_{\delta}(k|M,z)\right] P^{\mathrm{lin}}(k,z), \tag{14}$$

where $P^{\mathrm{lin}}$ is the linear matter power spectrum, $b_{\mathrm{h}}$ is the linear bias (taken from the model of ref. [39]), and $\hat{u}_{\delta}(k|M,z)$ is the Fourier transform of the matter halo density profile, i.e. $\rho_{\mathrm{h}}(\boldsymbol{x}|M,z)/\bar{\rho}_{\mathrm{DM}}$. The Fourier transform of the $\gamma$-ray emission profile from annihilating dark matter is described by $\hat{v}_{\gamma_{\mathrm{DM}}}(k|M,z)$, and it is related to the square of the dark matter density profile. For its precise form, see the appendix of ref. [49].

*Astrophysical $\gamma$-ray sources*

The cross-correlation of the matter density with astrophysical $\gamma$-ray sources is given by the 3D power spectrum:

$$P^{1\mathrm{h}}_{\gamma_{\mathrm{S}}\delta}(k,z) = \int_{\mathcal{L}_{\mathrm{min}}}^{\mathcal{L}_{\mathrm{max}}} \mathrm{d}\mathcal{L} \, \frac{\Phi_{\mathrm{S}}(\mathcal{L},z)}{\langle f_{\mathrm{S}}\rangle} \frac{\mathrm{d}F}{\mathrm{d}E}(\mathcal{L},z) \, \hat{u}_{\delta}\left[k|M(\mathcal{L},z),z\right] \tag{15}$$

$$P^{2\mathrm{h}}_{\gamma_{\mathrm{S}}\delta}(k,z) = \left[\int_{\mathcal{L}_{\mathrm{min}}}^{\mathcal{L}_{\mathrm{max}}} \mathrm{d}\mathcal{L} \, b_{\mathrm{S}}(\mathcal{L},z) \, \frac{\Phi_{\mathrm{S}}(\mathcal{L},z)}{\langle f_{\mathrm{S}}\rangle} \frac{\mathrm{d}F}{\mathrm{d}E}(\mathcal{L},z)\right] \left[\int_{M_{\mathrm{min}}}^{M_{\mathrm{max}}} \mathrm{d}M \, \frac{\mathrm{d}n}{\mathrm{d}M} b_{\mathrm{h}}(M,z) \hat{u}_{\delta}(k|M,z)\right] P^{\mathrm{lin}}(k,z), \tag{16}$$

where $b_{\mathrm{S}}$ is the bias of $\gamma$-ray astrophysical sources with respect to the matter density, for which we adopt $b_{\mathrm{S}}(\mathcal{L},z) = b_{\mathrm{h}}[M(\mathcal{L},z)]$. That is, a source with luminosity $\mathcal{L}$ has the same bias $b_{\mathrm{h}}$ as a halo with mass $M$, with the relation $M(\mathcal{L},z)$ between the mass of the host halo $M$ and the luminosity of the hosted object $\mathcal{L}$ taken from ref. [2]. The mean flux $\langle f_{\mathrm{S}}\rangle$ is defined as $\langle f_{\mathrm{S}}\rangle = \int \mathrm{d}\mathcal{L}\mathrm{d}F/\mathrm{d}E\Phi_{\mathrm{S}}$.

## BLINDING AND UNBLIDING PROCEDURE

The analysis has been performed by adopting a blinding technique, which relied on the execution of the cross-correlation analysis on nine combinations of data – one true and the other artificial. For both $\gamma$-rays and gravitational lensing we adopted 3 data variants, one of which was the true one. After the data were created, they were randomly assigned symbolic names. The analysis was then performed on all 9 combinations of data, without knowing which was the true version.

The aim of the blinding was to ensure that our analysis would not falsely detect a signal. Criteria to test the blind analysis were defined beforehand. After recording the results of the blind analysis and agreeing on its interpretation, the symbolic name assignments were revealed.

The construction of the versions of the data and the unblinding procedure is discussed below.

### Blinded $\gamma$-ray maps

The $\gamma$-ray maps adopted in the blind analysis are:

- G0: The true *Fermi*-LAT $\gamma$-ray maps.
- G1: Poissonian random map with a constant expected photon count over all the unmasked pixels, i.e. in each pixel of the map we extract a random number from a Poissonian distribution with fixed mean. The mean was computed by taking the average counts of the real maps in the unmasked pixels in each energy bin, and then multiplying it by a factor of 10 in order to simulate improved statistics. The produced counts maps are then transformed into flux maps by the usual procedure of dividing them by the mean detector exposure in each energy bin and by the pixel area.

- G2: Random reshuffle of all unmasked pixels of the real map in each energy bin.

Once produced, the three sets of maps have been blindly and randomly assigned names A, B and C and the association stored.

### Blinded shear maps

The shear signals adopted in the blind analysis are:

- K0: The true DES tangential component of galaxy shapes (this is the shear component for which we are looking for the cross-correlation signal when combined with the *Fermi* maps).
- K1: The cross-component (also known as $B$-modes or $\gamma_\times$) of galaxy shapes (which instead should yield pure shape noise and a null detection when correlated with the *Fermi* maps).
- K2: A linear combination of the null signal given by K1 and the cross-correlation signal of REDMAGIC galaxies at redshift $z = 0.2 - 0.45$ [51], with the linear combination coefficients chosen such that the signal should be neither plainly visible nor certainly undetectable. Since the correlation between REDMAGIC galaxies and gravitational shear is significant, this mock data set is meant to inject in our analysis a situation potentially (but not necessarily) leading to what could be seen as a detection.

Once produced, the three versions of the data have been blindly and randomly assigned names X, Y and Z and the association stored. We note here that the case K1 provides the cross-shear null test investigated in previous attempts of measurement of the signal [3–6].

### Blind analysis and unblinding procedure

The nine versions of cross-correlations results were all processed and vetted, with no team member aware of which combination represented the true data vector. We proceeded to the unblinding only once a number of (previously defined) criteria where satisfied: essentially, we needed to have at least one set for each $\gamma$-ray map compatible with noise (because of K1) and one with some (possibly weak) signal (because of K2). This has been done by evaluating the $\chi^2$ differences defined in the main text as the statistical estimator. In order to evaluate the statistical significance of the obtained $\Delta\chi^2$, we derived the distribution of various cases from multivariate Gaussian realizations. In the following, we summarise the main and most relevant results.

We note one substantial change to the analysis after unblinding. Tests with versions of the *Fermi*-LAT data that differ in the subtraction of a Galactic foreground model revealed a bug in our treatment of weak lensing shear around pixels with negative foreground-subtracted flux. All results in the main text of this paper have been updated, leading to an increase in signal-to-noise ratio from 4.5 to 5.3. The error did not affect our unblinding choices, particularly because it did not affect shear measurements around the G1 and G2 maps, which have no pixels with negative flux.

The $\Delta\chi^2$ between null signal and models for all the combinations analyzed are reported in Table I, for both the *phenomenological* and *physical* models. By looking at the *phenomenological* model analysis, the table shows that the majority of cases have a very low $\Delta\chi^2$, as expected from the combination of the data sets discussed in the previous Sections. Specifically, for each of the versions of the blinded $\gamma$-ray maps, at least one of the three shear data vectors is consistent with pure shape noise. Two cases exhibit a somewhat large $\Delta\chi^2$: AZ and CX. There are two possibilities in the subsets data combination that could provide such a situation: the combination of any version of the $\gamma$-ray map with the REDMAGIC galaxy signal or the combination of the true *Fermi* and the true DES data, if a signal is in fact present (combination G0-K0). These results, as well as those discussed below, remain valid also after the post-unblinding correction mentioned above.

By looking at the *physical* case results, we notice that the largest $\Delta\chi^2$'s occur for CX, while AZ is consistent with no signal. The fact that AZ cannot be fitted by the *physical* model implies this case does not provide a real signal. Let's comment that in this part of the analysis, for the *physical* case we used a reference model (further discussed in the next Section) which assumes for simplicity the normalisation of the 1-halo and 2-halo terms for blazars to be equal ($A^{\rm 1h}_{\rm BLZ} = A^{\rm 2h}_{\rm BLZ}$) and which refers to a DM particle annihilating into hadronic states, specifically into a $\bar{b}b$ pair. The null $\chi^2$ distribution and the distribution of expected $\Delta\chi^2$ for the reference *physical* model are reported in Fig. 8. They are obtained by drawing from a multivariate Gaussian with mean given by the reference model and covariance given

| | Map combination | | | | | | | | |
|---|---|---|---|---|---|---|---|---|---|
| | AX | AY | AZ | BX | BY | BZ | CX | CY | CZ |
| $\Delta\chi^2_{\rm phe}$ | 1.17 | 0.27 | 29.3 | 4.09 | 0.26 | 0.60 | 27.5 (21.1) | 1.56 (1.27) | 1.50 (1.90) |
| $\Delta\chi^2_{\rm phys}$ | −0.06 | 0.04 | 2.58 | 3.09 | −0.02 | 3.33 | 18.2 (9.91) | 0.65 (0.15) | 2.06 (1.72) |

TABLE I: $\Delta\chi^2_{\rm mod}$ computed for the *physical* and *phenomenological* models with respect to the null hypothesis for the various combinations of the blind analysis. Only the combination of true $\gamma$-ray and shear data (CX) and the low-noise mock $\gamma$-ray map with an injected artificial shear signal (AZ) show a large preference for the model vs the null hypothesis (no signal). The *physical* model adopted in the blind analysis is the reference model discussed in the text. For CX, CY and CZ, we show in parenthesis also the values considered in the blinding phase, before the post-unblinding correction mentioned in the text.

by the same covariance used in the data analysis. The null $\chi^2$ distribution peaks around 433. The $\Delta\chi^2$ distribution is rather broad and implies that $\Delta\chi^2$ of all variants reported in Table I are potentially compatible with the true case, since their $\Delta\chi^2$ is well inside the distribution in Fig. 8. The peak of the distribution indicates that the expected $\Delta\chi^2$ for the reference model is around 28. Fig. 8 shows as shaded areas the $\chi^2$ and $\Delta\chi^2$ distributions obtained before the post-unblinding correction was applied. No difference is obtained for the $\chi^2$, while for the $\Delta\chi^2$ a distribution peaked at larger values of $\Delta\chi^2$ is obtained after applying the correction, as a consequence of the increased sensitivity to the presence of a signal. The results are consistent with their mutual data sets and show that the bug did not lead to erronoeus conclusions.

The unblinding revealed the following identifications: A → G1, B → G2, C → G0, X → K0, Y → K1, Z → K2. The coefficients of the linear combination in K2 were such that the injected signal was rather small, and therefore not easily identifiable. Moreover, being a signal due to the cross-correlation between the galaxy distribution and gravitational shear, it does not have to be compatible with our *physical* models (constructed specifically for the cross-correlation with $\gamma$-rays), while instead it could be well described by the *phenomenological* model (since it contains a generic 1-halo and 2-halo terms).

From all these considerations, we see first of all that the results shown in Table I are fully compatible with expectations: there is no "spurious" detection, while the presence of a signal occurs only for those cases for which this is potentially possible. In fact, the CX case (the one corresponding to the combination of the true *Fermi* and DES data) is the only one that presents a high $\Delta\chi^2$ for both the *phenomenological* and *physical* model. The $\Delta\chi^2$ is larger in the case of the *phenomenological* model since the latter has more freedom to adapt to data. CY and CZ are compatible with null signal. The smallness of the injected signal in Z makes this case essentially indistinguishable from pure noise. Finally, the null $\chi^2$ for CX is 468, compatible with the expectations of the distribution of Fig. 8.

None of the combinations involving A and B maps present a statistically significant $\Delta\chi^2$ either with respect to the *physical* or the *phenomenological* model, except for the *phenomenological* fit for the AZ case. We remind that map A is built from Poissonian $\gamma$-ray noise with enhanced photon count statistics. The latter means that the size of the errors is significantly reduced, and now the "small" injected signal is enough to provide a significant detection. On the other hand, the "artificial" nature of the signal is revealed by the fact that the *physical* model is not able to fit it. The freedom we left to the *phenomenological* model is instead large enough to make it able to include the signal of cross-correlation with galaxies.

In the next Section we outline the specifications of the reference model used for the blind analysis.

## REFERENCE MODEL

In the pipeline of the analysis before unblinding, we adopted a *physical* model with blazars, mAGN, SFG and DM annihilating into a $\bar{b}b$ pair, with a common normalization for the 1-halo and 2-halo terms for blazars, i.e., $A^{\rm 1h}_{\rm BLZ} = A^{\rm 2h}_{\rm BLZ}$. This was the first obvious options, since it adopts a nominal model for the blazar terms and minimises the number of free parameters. As seen from the triangle plot in Fig. 9, the parameter scan for the CX case provides upper bounds for the three astrophysical components and a hint for the presence of a DM signal is found at the $3.1\sigma$ C.L., with best-fit parameters $m_{\rm DM} = 302$ GeV and normalization of the annihilation cross section relative to the natural scale $A_{\rm DM} = 105$. Overall, the statistical significance of this reference *physical* model is SNR = 4.2, with $\Delta\chi^2$= 18.2 (for brevity, in this Section, we only quote the significance obtained after the post-unbliding correction mentioned above).

In the right panel of Fig. 9, we show the cross-correlation signal for the best fit of this reference *physical* model, compared to the data points. While large scales are well fitted by the model, a clear lack of power is present at small

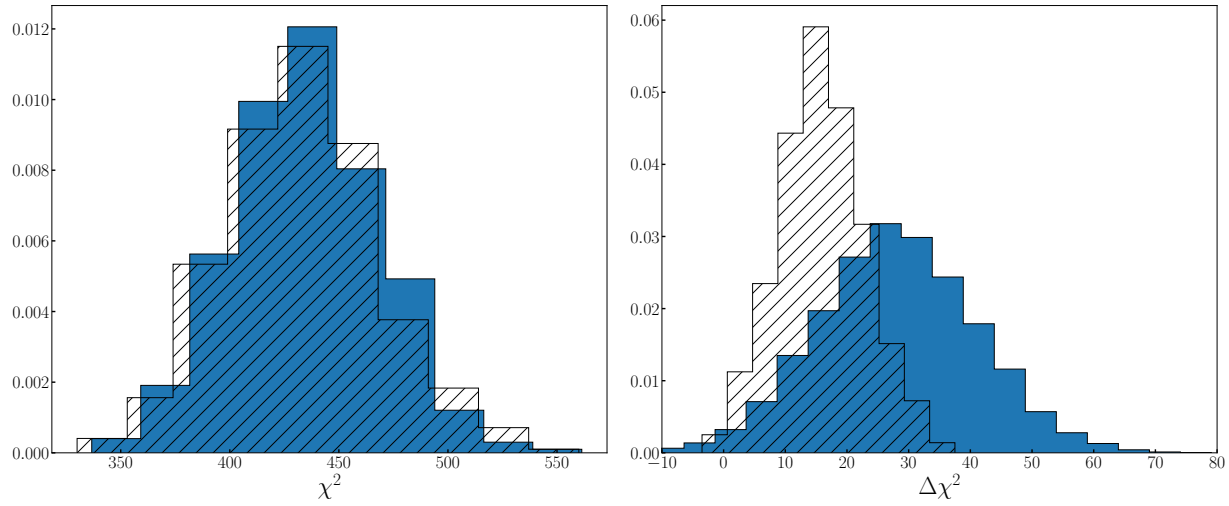


FIG. 8: Distribution of the expected $\chi^2$ (left) and $\Delta\chi^2$ (right) for the reference *physical* model used in the Monte Carlo Markov Chain analysis during the blind phase (shades areas) and the same distributions obtained after the post-unbliding correction mentioned above (blue areas). The normalization of the components in the model were chosen in order to reproduce the total UGRB emission. The meaning of the plot is to show the expectations for the null $\chi^2$ with the way of estimating the covariance used in this work, and for the $\Delta\chi^2$ of the true case for the purpose of blinded tests. The $\Delta\chi^2$ should be compared to the values reported in the second line of Table I.

angular scales. From Fig. 2 of the main text we instead know that in the *phenomenological* model, the PSF-like 1-halo term can account for the measured CCF at small scales properly. This implies that the reference model, in its simplest formulation, is excessively limiting the ability to adapt to the data: a larger 1-halo term is needed.

Considering that the data require a hard-spectrum, not compatible with astrophysical components other than blazars, we improve the modelling by allowing the 1-halo and 2-halo terms for blazars to be independently normalised. In this case, the small scale correlation is well fitted, and a peak in the posterior distribution for the 1-halo blazar component arises (see Fig. 3 of the main text). This improves the SNR from 4.2 to 5.2, while the dark matter component loses some of its significance with respect to the original reference case.

We have also investigated variations of the dark matter model in terms of considering different annihilation channels, as it is usually done in dark matter analyses. We found a preference for leptonic annihilation, with the preferred option being annihilation into $\tau$-lepton pairs: this increases the global SNR to 5.2, with a preference for the presence of a dark matter signal at the $2.8\sigma$ confidence level. This is the model that we report in the main text. In the case the DM component is not included, we obtain $\Delta\chi^2 = 16.5$, as compared to $\Delta\chi^2 = 27$ for the case with DM.

Concerning the blazar 1-halo component, this depends on the relation between the blazar luminosity and the host-halo mass, as can be seen in Eq. 15. In the reference model used for the blind analysis this relation has been taken from ref. [2], where it was derived by linking the $\gamma$-ray luminosity of a blazar to the mass of the supermassive black hole powering the AGN and then relating the mass of the black hole to the mass of the DM halo. Combining these pieces together, this peocedure gives $M(\mathcal{L}) = 2 \times 10^{13} M_\odot \, (\mathcal{L}/10^{47} \mathrm{erg\,s^{-1}})^{0.23} (1+z)^{-0.9}$, where $\mathcal{L}$ is the rest-frame luminosity of blazars in the energy range 0.1 to 100 GeV. Assuming this relation to be a power-law and fixing the redshift dependence as in the reference model (since, as we already mentioned, it is weakly constrained by data, and we therefore do not gain meaningful insight from the fit), we explore in the left panel of Fig. 10 which $M(\mathcal{L})$ relation would be needed in order to reproduce the 1-halo term of our refined model. The plot shows the best-fit relation and its 68% C.L. contours in the plane $(\alpha, M_0)$ for a relation $M(\mathcal{L}) = M_0 \, (\mathcal{L}/10^{47} \mathrm{erg\,s^{-1}})^{\alpha} (1+z)^{-0.9}$. Our results suggest the average mass of a halo hosting a blazar is larger than the one adopted in [2], and most likely above $10^{14} M_\odot$. The cross-correlation signal with weak lensing seems therefore to be dominated by blazars residing in cluster-size halos. In the right panel of Fig. 10, we show with a few examples that modifying the $M(\mathcal{L})$ relation has a dramatic impact on the the 1-halo power spectrum, while it only mildly affects the 2-halo term.

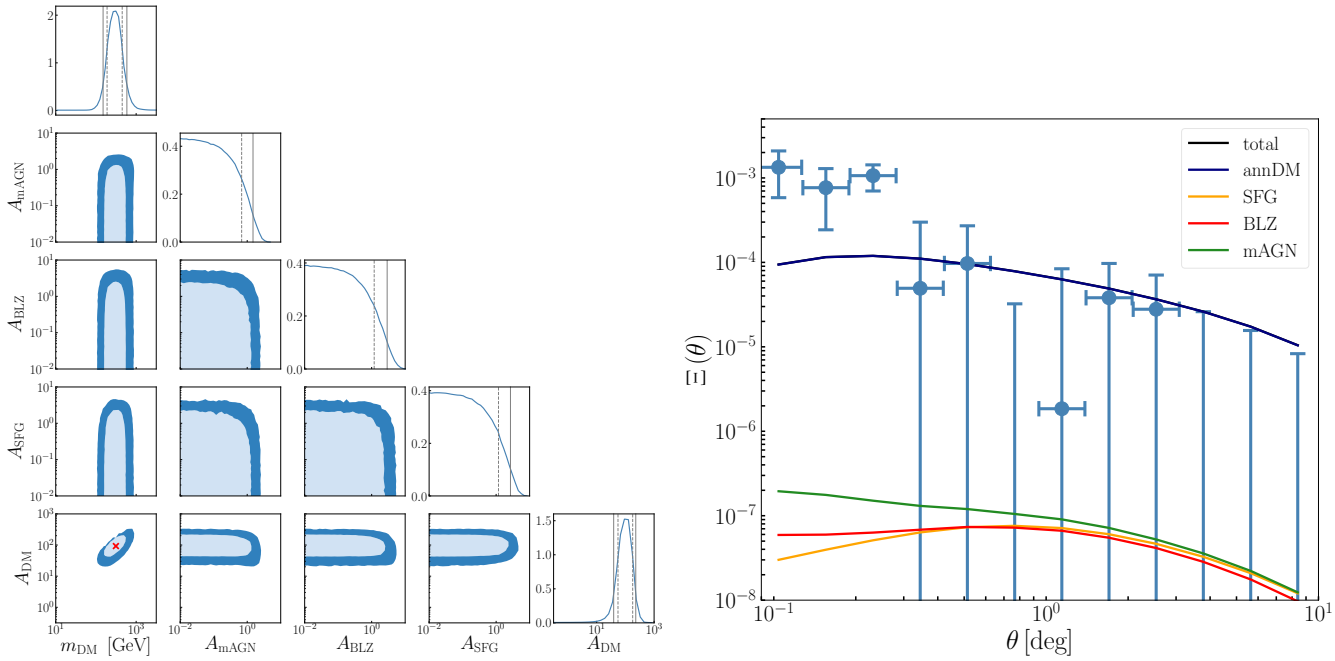


FIG. 9: Left: Triangle plot for the normalisation parameters and dark matter mass of the reference *physical* model described in the text. The model incorporates star-forming galaxies, blazars, misaligned AGNs, and a dark matter candidate annihilating in the $b\bar{b}$ channel. The parameters are presented in log-scale. The 1D profile likelihood distributions are normalised to unity. The dashed and solid lines represent, respectively, the 68% and 95% CL limits obtained in the Monte Carlo parameter scan. Same contour levels for the light and dark blue regions in the 2D distributions. Right: The blue dots show the integrated cross-correlation function obtained by averaging over all redshift and energy bins. The error bars are obtained from the diagonal terms of the covariance matrix, summed in quadrature. Lines show the integrated best-fit CCF for the *physical reference* model. The blue, orange, red and green lines correspond to the dark matter star-forming galaxies, blazars, and misaligned AGNs contributions, respectively.


[1] Fornengo, N., & Regis, M. Particle dark matter searches in the anisotropic sky. *Frontiers in Physics* **2**, 6 (2014)

[2] Camera, S., Fornasa, M., Fornengo, N., & Regis, M. Tomographic-spectral approach for dark matter detection in the cross-correlation between cosmic shear and diffuse $\gamma$-ray emission. *JCAP* **1506**, 029 (2015)

[3] Shirasaki, M., Horiuchi, S., & Yoshida, N. Cross correlation of cosmic shear and extragalactic gamma-ray background: Constraints on the dark matter annihilation cross section. *Phys. Rev. D* **90**, 063502 (2014)

[4] Shirasaki, M., Macias, O., Horiuchi, S., Shirai, S., & Yoshida, N. Cosmological constraints on dark matter annihilation and decay: Cross-correlation analysis of the extragalactic $\gamma$-ray background and cosmic shear. *Phys. Rev. D* **94**, 063522 (2016)

[5] Tröster, T., Camera, S., Fornasa, M., et al. Cross-correlation of weak lensing and gamma rays: implications for the nature of dark matter. *Mon. Not. Roy. Astron. Soc.* **467**, 2706 (2017)

[6] Shirasaki, M., Macias, O., Horiuchi, S., et al. Correlation of extragalactic $\gamma$ rays with cosmic matter density distributions from weak gravitational lensing. *Phys. Rev. D* **97**, 123015 (2018)

[7] Gruen, D., et al. Density split statistics: Cosmological constraints from counts and lensing in cells in DES Y1 and SDSS data. *Phys. Rev. D* **98**, 023507 (2018)

[8] Sheldon, E. S., & Huff, E. M. Practical Weak-lensing Shear Measurement with Metacalibration. *Astrophys. J.* **841**, 24 (2017)

[9] Zuntz, J., et al. Dark Energy Survey Year 1 Results: Weak Lensing Shape Catalogues. *Mon. Not. Roy. Astron. Soc.* **481**, 1149 (2018)

[10] Ackermann, M., et al. Unresolved Gamma-Ray Sky through its Angular Power Spectrum. *Phys. Rev. Lett.* **121**, 241101 (2018)

[11] Moliné, Á., Schewtschenko, J. A., Palomares-Ruiz, S., Boehm, C., & Baugh, C. M. Isotropic extragalactic flux from dark matter annihilations: lessons from interacting dark matter scenarios. *JCAP* **1608**, 069 (2016)

[12] Hiroshima, N., Ando, S., & Ishiyama, T. Modeling evolution of dark matter substructure and annihilation boost. *Phys. Rev. D* **97**, 123002 (2018)

[13] Dark Energy Survey Collaboration. The Dark Energy Survey: more than dark energy - an overview. *Mon. Not. Roy.*

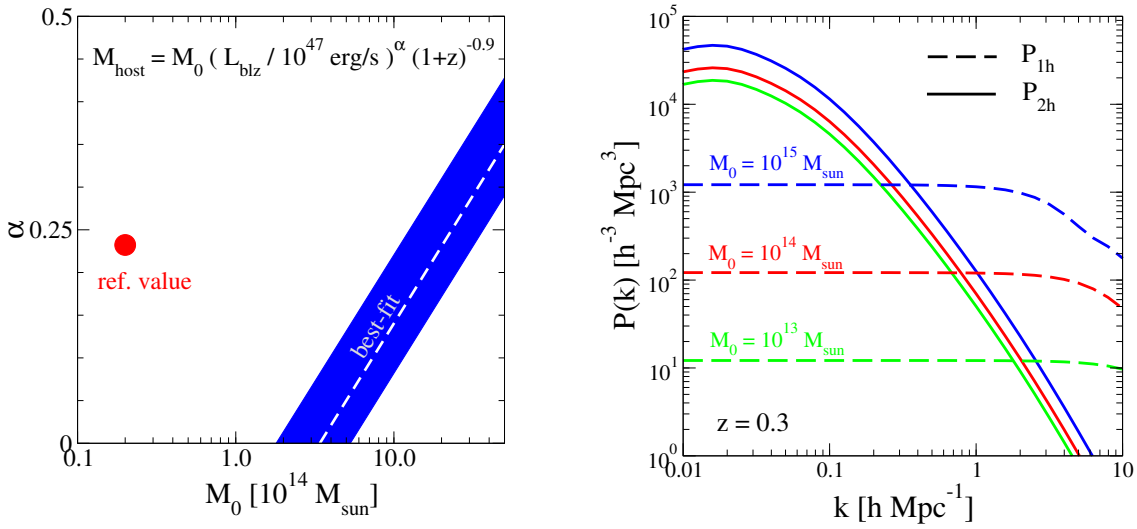


FIG. 10: Left: The blue region shows the 68% C.L. interval for the parameters $\alpha$ and $M_0$ describing the blazar luminosity versus host-halo mass relation. Red dot reports the combination adopted for the reference model described in the text. Right: Power spectrum of cross-correlation between $\gamma$-ray emission from blazars and shear at $z = 0.3$ for different choices of the $M(\mathcal{L})$ relation. We show separately the 1-halo (dashed) and 2-halo terms (solid). For definiteness, we keep $\alpha$ fixed to 0.23 and vary only $M_0$.


*Astron. Soc.* **460**, 1270 (2016)

[14] Flaugher, B., et al. The Dark Energy Camera. *Astron.J.* **150**, 150 (2015)

[15] Diehl, H. T., et al. The Dark Energy Survey and Operations: Year 1. *Proc. SPIE Int. Soc. Opt. Eng.* **9149**, 91490V (2014)

[16] Drlica-Wagner, A., et al. Dark Energy Survey Year 1 Results: The Photometric Data Set for Cosmology. *Astrophys. J. Suppl.* **235**, 33 (2018)

[17] Annis, J., Soares-Santos, M., Strauss, M. A., et al. The Sloan Digital Sky Survey Coadd: 275 deg$^2$ of Deep Sloan Digital Sky Survey Imaging on Stripe 82. *Astrophys. J.* **794**, 120 (2014)

[18] Carlstrom, J. E., et al. The 10 Meter South Pole Telescope. *Publ.Astron.Soc.Pac.* **123**, 568 (2011)

[19] Huff, E., & Mandelbaum, R. Metacalibration: Direct Self-Calibration of Biases in Shear Measurement. Preprint `https://arxiv.org/abs/1702.02600` (2017)

[20] Benítez, N. Bayesian Photometric Redshift Estimation. *Astrophys. J.* **536**, 571 (2000)

[21] Hoyle, B., et al. Dark Energy Survey Year 1 Results: Redshift distributions of the weak lensing source galaxies. *Mon. Not. Roy. Astron. Soc.* **478**, 592 (2018)

[22] Ajello, M., et al. 3FHL: The Third Catalog of Hard Fermi-LAT Sources. *Astrophys. J. Suppl.* **232**, 18 (2017)

[23] Hikage, C., Oguri, M., Hamana, T., et al. Cosmology from cosmic shear power spectra with Subaru Hyper Suprime-Cam first-year data. *Publ.Astron.Soc.Jap.* **71**, 2 (2019)

[24] Murata, R., Nishimichi, T., Takada, M., et al. Constraints on the mass-richness relation from the abundance and weak lensing of SDSS clusters. *Astrophys. J.* **854**, 120 (2018)

[25] Fornasa, M., et al. Angular power spectrum of the diffuse gamma-ray emission as measured by the Fermi Large Area Telescope and constraints on its dark matter interpretation. *Phys. Rev. D* **94**, 123005 (2016)

[26] Planck Collaboration. Ade, P. A. R., Aghanim, N., et al. Planck 2015 results. XIII. Cosmological parameters. *Astron.Astrophys.* **594**, A13 (2016)

[27] Troxel, M. A., MacCrann, N., Zuntz, J., et al. Dark Energy Survey Year 1 results: Cosmological constraints from cosmic shear. *Phys. Rev. D* **98**, 043528 (2018)

[28] Anderson, T. An Introduction To Multivariate Statistical Analysis, 3rd ed. (Wiley India Pvt. Limited, 2009)
[29] Hartlap, J., Simon, P., & Schneider, P. Why your model parameter confidences might be too optimistic. Unbiased estimation of the inverse covariance matrix. *Astron.Astrophys.* **464**, 399 (2007)
[30] Kilbinger, M., Fu, L., Heymans, C., et al. CFHTLenS: Combined probe cosmological model comparison using 2D weak gravitational lensing. *Mon. Not. Roy. Astron. Soc.* **430**, 2200 (2013)
[31] Troxel, M. A., Krause, E., Chang, C., et al. Survey geometry and the internal consistency of recent cosmic shear measurements. *Mon. Not. Roy. Astron. Soc.* **479**, 4998 (2018)
[32] S. Ammazzalorso, N. Fornengo, S. Horiuchi and M. Regis, Phys. Rev. D **98**, no. 10, 103007 (2018)
[33] Bartelmann, M. Gravitational Lensing. *Classical and Quantum Gravity* **27**, 233001 (2010)
[34] Ando, S., & Komatsu, E. Anisotropy of the cosmic gamma-ray background from dark matter annihilation. *Phys. Rev. D* **73**, 023521 (2006)
[35] Fornengo, N., Pieri, L., & Scopel, S. Neutralino annihilation into $\gamma$ rays in the Milky Way and in external galaxies. *Phys. Rev. D* **70**, 103529 (2004)
[36] Cembranos, J. A. R., de La Cruz-Dombriz, A., Dobado, A., Lineros, R. A., & Maroto, A. L. Photon spectra from WIMP annihilation. *Phys. Rev. D* **83**, 083507 (2011)
[37] Cirelli, M., Corcella, G., Hektor, A., et al. PPPC 4 DM ID: A Poor Particle Physicist Cookbook for Dark Matter Indirect Detection. *JCAP* **3**, 051 (2011)
[38] Finke, J. D., Razzaque, S., & Dermer, C. D. Modeling the Extragalactic Background Light from Stars and Dust. *Astrophys. J.* **712**, 238 (2010)
[39] Sheth, R. K., & Tormen, G. Large-scale bias and the peak background split. *Mon. Not. Roy. Astron. Soc.* **308**, 119 (1999)
[40] Navarro, J. F., Frenk, C. S., & White, S. D. M. A Universal Density Profile from Hierarchical Clustering. *Astrophys. J.* **490**, 493 (1997)
[41] Prada, F., Klypin, A. A., Cuesta, A. J., Betancort-Rijo, J. E., & Primack, J. Halo concentrations in the standard LCDM cosmology. *Mon. Not. Roy. Astron. Soc.* **423**, 3018 (2012)
[42] Sánchez-Conde, M. A., & Prada, F. The flattening of the concentration-mass relation towards low halo masses and its implications for the annihilation signal boost. *Mon. Not. Roy. Astron. Soc.* **442**, 2271 (2014)
[43] Ajello, M., Gasparrini, D., Sánchez-Conde, M., et al. The Origin of the Extragalactic Gamma-Ray Background and Implications for Dark Matter Annihilation. *Astroph. J. Lett.* **800**, L27 (2015)
[44] Acero, F., et al. Fermi Large Area Telescope Third Source Catalog. *Astrophys. J. Suppl.* **218**, 23 (2015)
[45] Di Mauro, M., Calore, F., Donato, F., Ajello, M., & Latronico, L. Diffuse $\gamma$-ray emission from misaligned active galactic nuclei. *Astrophys. J.* **780**, 161 (2014)
[46] Gruppioni, C., Pozzi, F., Rodighiero, G., et al. The Herschel PEP/HerMES Luminosity Function. I: Probing the Evolution of PACS selected Galaxies to z$\sim$4. *Mon. Not. Roy. Astron. Soc.* **432**, 23 (2013)
[47] Ackermann, M., Ajello, M., Allafort, A., et al. GeV Observations of Star-forming Galaxies with the Fermi Large Area Telescope. *Astroph. J.* **755**, 164 (2012)
[48] Cooray, A., & Sheth, R. Halo models of large scale structure. *Phys. Rep.* **372**, 1 (2002)
[49] Cuoco, A., Xia, J.-Q., Regis, M., et al. Dark matter searches in the gamma-ray extragalactic background via cross-correlations with galaxy catalogues. *Astrophys. J. Suppl.* **221**, 29 (2015)
[50] J. Q. Xia, A. Cuoco, E. Branchini and M. Viel, Astrophys. J. Suppl. **217**, no. 1, 15 (2015)
[51] Prat, J., Sánchez, C., Fang, Y., et al. Dark Energy Survey year 1 results: Galaxy-galaxy lensing. *Phys. Rev. D* **98**, 042005 (2018)
[52] `https://fermi.gsfc.nasa.gov/ssc/data/analysis/software/`
[53] See `http://www.slac.stanford.edu/exp/glast/groups/canda/lat\protect\_Performance.htm`
[54] `https://fermi.gsfc.nasa.gov/ssc/data/analysis/documentation/Cicerone/Cicerone\protect\_LAT\protect\_IRFs/index.html`
[55] `https://fermi.gsfc.nasa.gov/ssc/data/access/lat/fl8y/`
[56] `https://fermi.gsfc.nasa.gov/ssc/data/access/lat/BackgroundModels.html`